

Pure Spin Photocurrent in Non-centrosymmetric Crystals:

Bulk Spin Photovoltaic Effect

Haowei Xu ¹, Hua Wang ¹, Jian Zhou ¹, and Ju Li ^{1,2 †}

¹ Department of Nuclear Science and Engineering, Massachusetts Institute of Technology,
Cambridge, Massachusetts 02139, USA

² Department of Materials Science and Engineering, Massachusetts Institute of Technology,
Cambridge, Massachusetts 02139, USA

Abstract

The shift current and the circular current can generate charge currents under light illumination via nonlinear optical (NLO) interaction, and are called bulk photovoltaic effect (BPVE) and the circular photogalvanic effect (CPGE), respectively. In this work, we reveal that the similar mechanisms can be applied to spin currents and demonstrate a unified picture of NLO charge and spin currents generation. We show that in some cases, the net charge current is zero due to symmetry constraints, but there are still hidden carrier movements, which can be measured if the spin degree of freedom is considered and can lead to a hidden *pure* spin current. Symmetry analysis reveals that the NLO spin current can be generated under both linearly and circularly polarized light in any non-centrosymmetric materials regardless of whether time reversal symmetry (magnetism) exists or not. And a pure spin current can be realized if the system possesses additional mirror symmetry or inversion-mirror symmetry. We apply our theory to several distinct material systems with easy optical accessibility, namely, two-dimensional transition metal dichalcogenides (TMD), anti-ferromagnetic MnBi_2Te_4 (MBT), and the surface states of topological material SnTe. The spin current conductivity is found to be gigantic, often exceeding BPVE. Such bulk spin photovoltaic effect (BSPE) could find wide applications in energy efficient and ultrafast spintronic devices.

[†] correspondence to: liju@mit.edu

Introduction. Electronics, which utilizes the charge degree of freedom of electrons, has revolutionized human civilization. Beside charge, spin is yet another intrinsic degree of freedom of electrons that can be exploited. Spintronics^{1,2} is a promising candidate for next generation energy-efficient devices and other novel applications such as quantum computing^{3,4} and neuromorphic computation⁵. One of the core challenges⁶ of spintronics is the generation of the spin current, and particularly, a *pure* spin current without an accompanying charge current. Until now, there have been a few approaches, such as the interconversion between charge and spin currents by (inverse) spin galvanic effect^{7,8} or (inverse) spin Hall effect⁹⁻¹², and the interconversion between thermal and spin currents by spin Seebeck effect^{13,14} or spin Nernst effect^{15,16}, etc. These approaches require mechanical or electrical contact and patterning, and the response time is usually on the order of nanoseconds and above. These issues can be resolved with optical approaches, which do not require direct contact and are noninvasive, and can enable ultrafast response time on the order of picoseconds and below. Actually, several optical approaches for generating spin current have been proposed. However, these approaches usually require the breaking of time reversal symmetry \mathcal{T} , either by the circularly polarized light (CPL), or by the material system itself (e.g., magnetic materials). For example, CPL can selectively couple with spin-up and down states in quantum wells¹⁷, quantum interfering^{18,19} or spin-valley locked systems²⁰, and the imbalanced population of spin up and down states could lead to a spin photocurrent. It has also been proposed that in \mathcal{T} -broken material systems, a linearly polarized light (LPL) can generate a spin current with the shift-current mechanism^{21,22}. Although some progress has been made, generation of spin current under light is still in its infancy. In particular, it is highly desirable to have new mechanisms applicable to a broader family of materials, preferably without any stringent requirements on the material itself such as broken \mathcal{T} , or any external manipulations such as quantum interference.

In this work, we propose a bulk spin photocurrent induced by a nonlinear optical (NLO) effect, which is applicable to both LPL and CPL. Also, such an NLO spin current requires only the breaking of inversion symmetry \mathcal{P} , and is regardless of \mathcal{T} . Therefore, it can be obtained in typical nonmagnetic semiconductors such as GaAs under LPL. Actually, this NLO spin photocurrent is the cousin of the bulk photovoltaic effect (BPVE) and the circular photogalvanic effect (CPGE) for charge current generation under light. The BPVE, or the *shift* current, has potential applications in energy harvesting and photon detection, while the CPGE, also known as the circular current or the *injection* current, is under intensive research as well²³⁻²⁷. The shift and injection mechanisms

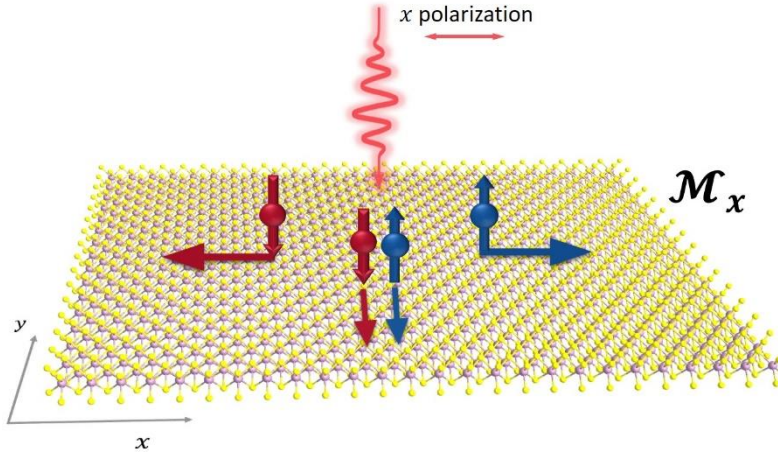


Figure 1. A schematic illustration of pure spin and charge current. The light polarizes in the x direction, while the system has mirror symmetry \mathcal{M}^x . In the x direction, spin up and down states travel in opposite directions, so that the net charge current is vanishing, whereas the net spin current goes to the $+x$ direction. In the y direction, spin up and down electrons travel in the same direction, leading to non-vanishing charge current but vanishing spin current.

are widely studied, but by far the attention is mainly on the charge current, while the spin current has long been neglected. Certainly, when the charge flows under light, the spin associated with the carriers are moving as well, thus a spin current should be generated together with the charge current. In some situations, the charge current may vanish due to symmetry constraints, but this does not indicate that carriers are frozen in materials. Instead, the carriers are still moving and there can be a nonzero spin current. Therefore, the hidden carrier movements can be revealed by the *pure* spin current. A generic picture here is that electrons with opposite spin polarizations travel in the opposite directions, so that the net charge current is vanishing while the net spin current is nonzero (Figure 1). From a different point of view, the electronic structure hidden in the nonlinear charge current could be uncovered when the spin degree of freedom is considered. Compared with other hidden physical effects that are hidden in real space, such as hidden spin polarization^{28,29}, the hidden current is actually hidden in the reciprocal space (\mathbf{k} -space). And the spin current could also be used to detect other hidden physical effects.

In order to demonstrate and evaluate the NLO spin current, we introduce a unified theory on NLO spin and charge currents generation and derive the general formula to calculate the conductivity. From symmetry analysis, we conclude that the generation of NLO spin current requires only \mathcal{P} breaking, regardless of \mathcal{T} . Furthermore, provided with mirror symmetry \mathcal{M} or

inversion-mirror symmetry \mathcal{PM} , a pure spin current can be realized, which is highly desirable for energy-efficient spintronics. We apply *ab initio* calculations to illustrate our theory in several distinct materials systems with easy optical accessibility, including nonmagnetic 2D transition metal dichalcogenides (TMD), anti-ferromagnetic (AFM) MnBi_2Te_4 (MBT), and the surface states of a topological insulating material SnTe. The results also indicate that the NLO spin current conductivity can be gigantic, that is even larger than the corresponding BPVE / CPGE charge current in the same system (in the sense of equivalating $\frac{\hbar}{2} = e$). We call this the Bulk Spin Photovoltaic Effect (BSPE). The BSPE mechanism is predicted to be an efficient way for spin current generation. Furthermore, spin current with arbitrary spin polarization can be realized, providing great flexibility for spintronics applications.

General Theory and Symmetry Analysis. The NLO charge or spin current under light with frequency ω can be expressed as

$$J^{a,s^i} = \sum_{\Omega=\pm\omega} \sigma_{bc}^{a,s^i}(0; \Omega, -\Omega) E^b(\Omega) E^c(-\Omega) \quad (1)$$

Here a, b, c are Cartesian indices and a indicates the direction of the current, while b and c are the polarization of the incident optical electric field. $E(\omega)$ is the Fourier component of the electric field at angular frequency ω . σ_{bc}^{a,s^i} is the NLO conductivity. s^i with $i = x, y, z$ is the spin polarization, while s^0 represents charge current. The spin and charge are in the unit of angular momentum $\frac{\hbar}{2}$ and electron charge e , respectively. In order to compare the charge and spin current conductivity values directly, we divide the spin current conductivity by a factor of $\frac{\hbar}{2e}$ ³⁰. We derived the formula for σ_{bc}^{a,s^i} from quadratic response theory^{31,32} (see Supplementary Materials, SM). Within the independent particle approximation, the conductivity can be expressed as

$$\begin{aligned} & \sigma_{bc}^{a,s^i}(0; \omega, -\omega) \quad (2) \\ & = -\frac{e^2}{\hbar^2 \omega^2} \text{Re} \left\{ \int \frac{d\mathbf{k}}{(2\pi)^3} \sum_{mnl} \phi_{bc} \frac{f_{lm} v_{lm}^b}{\omega_{ml} - \omega + i/\tau} \left(\frac{j_{mn}^{a,s^i} v_{nl}^c}{\omega_{mn} + i/\tau} - \frac{v_{mn}^c j_{nl}^{a,s^i}}{\omega_{nl} + i/\tau} \right) \right\} \end{aligned}$$

Here the explicit \mathbf{k} -dependence of the quantities are omitted. $f_{lm} = f_l - f_m$ and $\omega_{lm} = \omega_l - \omega_m$ are the difference between occupation number and band energy between bands l and m . $v_{nl} = \langle n | \hat{v} | l \rangle$ is the velocity matrix element, while τ is the carrier lifetime and is set as 0.2 ps in the

following. j^{a,s^i} with $i \neq 0$ is the spin current operator, defined as³³ $j^{a,s^i} = \frac{1}{2}(v^a s^i + s^i v^a)$. Here $s^i = \frac{\hbar}{2}\sigma^i$ is the spin operator with σ as the Pauli matrices. Note that if we define $s^0 = e$, then j^{a,s^0} would indicate the charge current. ϕ_{bc} is the phase difference between E^b and E^c , and LPL and CPL correspond to $\phi_{bc} = 1$ and $\phi_{bc} = \pm i$, respectively. Because the direct spin and charge current J^{a,s^i} should be a real quantity, the real (imaginary) part of σ_{bc}^{a,s^i} corresponds to the conductivity under LPL (CPL). The relation between Eq. (2) and the shift and injection mechanisms for current generation will be discussed in detail later. Note the Eq. (2) does not treat spin up and down states separately^{21,34} and can deal with arbitrary spin polarization under spin-orbit coupling (SOC). In practice, the Brillouin zone (BZ) integration in Eq. (2) is carried out by k -mesh sampling with $\int \frac{dk}{(2\pi)^3} = \frac{1}{V} \sum_k w_k$, where V is the volume of the simulation cell in real space and w_k is weight factor. However, for 2D materials, the definition of volume V is ambiguous, because the thickness of 2D materials is ambiguously defined³⁵. Thus, we replace volume V with the area S , and the 2D and 3D conductivity satisfy $\sigma_{2D} = L\sigma_{3D}$, where L is an effective thickness of the material.

Next, we consider symmetry constraints on the conductivity tensor. First we note that the numerators are composed of terms with format $N^{iabc} = s^i v^a v^b v^c$. Under spatial inversion operation \mathcal{P} , one has $\mathcal{P}v^a(\mathbf{k}) = -v^a(-\mathbf{k})$ and $\mathcal{P}s^i(\mathbf{k}) = s^i(-\mathbf{k})$. Thus $\mathcal{P}N^{iabc}(\mathbf{k}) = -N^{iabc}(-\mathbf{k})$, and all components (including charge and spin) of σ_{bc}^{a,s^i} should vanish after the BZ integration in \mathcal{P} -conserved systems. Therefore, the inversion symmetry \mathcal{P} has to be broken to have nonvanishing σ_{bc}^{a,s^i} . Regarding time reversal operation \mathcal{T} , one has $\mathcal{T}v^a(\mathbf{k}) = -v^{a*}(-\mathbf{k})$ and $\mathcal{T}s^i(\mathbf{k}) = -s^{i*}(-\mathbf{k})$ (Here \cdot^* indicates complex conjugate of \cdot). For charge current, one has $\mathcal{T}N^{0abc}(\mathbf{k}) = -N^{0abc*}(-\mathbf{k})$. Thus, only the *imaginary* part of $N^{0abc}(\mathbf{k})$ contributes to the total charge conductivity after BZ integration in a \mathcal{T} -conserved system. On the other hand, for spin- i current, one has $\mathcal{T}N^{iabc}(\mathbf{k}) = N^{iabc*}(-\mathbf{k})$, thus it is the *real* part of $N^{iabc}(\mathbf{k})$ that contributes to the total spin conductivity. Note that for both charge and spin current, \mathcal{T} does not need to be broken. Generally speaking, spin and charge currents should be generated simultaneously in the absence of \mathcal{P} . However, as we will show in detail later, a pure spin current can be realized if the system possesses mirror symmetry \mathcal{M}^d or inversion-mirror symmetry \mathcal{PM}^d . The behavior of several physical quantities under symmetry operations are summarized in Table 1.

In order to illustrate this theory, we investigate three typical but distinct material systems in the following: (1) a monolayer transition metal dichalcogenides (MoS₂) which is \mathcal{P} -broken but \mathcal{T} -preserved; (2) an antiferromagnetic bilayers MnBi₂Te₄ which is \mathcal{P} - and \mathcal{T} -broken but \mathcal{PT} -preserved; (3) surface state of a topological material (001-surface of SnTe) which has \mathcal{M}_x and \mathcal{M}_y but \mathcal{P} -broken. We only show the NLO charge and spin current under LPL, while the responses to CPL can be found in the SM.

Table 1 The behavior of physical quantities under symmetry operations. Here $\tilde{\cdot}$ indicates \cdot obtained on the \mathcal{PT} partner state, which is degenerate in energy with the original state. $[d; abc]$ is -1 if there are odd numbers of d within a, b and c and is $+1$ otherwise. For example, $[x; xxx] = -1$ while $[x; xxy] = 1$. $\mathbf{k}' = \mathcal{M}^d \mathbf{k}$ is the mirror image of \mathbf{k} , that is, only the d -th component of \mathbf{k} is flipped.

	$v^a(\mathbf{k})$	$s^i(\mathbf{k})$	$N^{0abc}(\mathbf{k})$	$N^{iabc}(\mathbf{k})$
\mathcal{P}	$-v^a(-\mathbf{k})$	$s^i(-\mathbf{k})$	$-N^{0abc}(-\mathbf{k})$	$-N^{iabc}(-\mathbf{k})$
\mathcal{T}	$-v^{a*}(-\mathbf{k})$	$-s^{i*}(-\mathbf{k})$	$-N^{0abc*}(-\mathbf{k})$	$N^{iabc*}(-\mathbf{k})$
\mathcal{PT}	$\tilde{v}^{a*}(\mathbf{k})$	$-\tilde{s}^{i*}(\mathbf{k})$	$\tilde{N}^{0abc*}(\mathbf{k})$	$-\tilde{N}^{iabc*}(\mathbf{k})$
\mathcal{M}^d	$(-1)^{\delta_{da}} v^a(\mathbf{k}')$	$-(-1)^{\delta_{di}} s^i(\mathbf{k}')$	$[d; abc]$ $\times N^{0abc}(\mathbf{k}')$	$-(-1)^{\delta_{di}} [d; abc]$ $\times N^{iabc}(\mathbf{k}')$
\mathcal{PM}^d	$-(-1)^{\delta_{ab}} v^a(-\mathbf{k}')$	$-(-1)^{\delta_{di}} s^i(-\mathbf{k}')$	$-[d; abc]$ $\times N^{0abc}(-\mathbf{k}')$	$(-1)^{\delta_{di}} [d; abc]$ $\times N^{iabc}(-\mathbf{k}')$

Monolayer Transition Metal Dichalcogenide. 2H phase TMDs, which lacks \mathcal{P} , are well studied 2D materials that possess many exotic electronic and optical properties. Particularly, monolayer TMDs exhibit Zeeman type spin splitting due to the in-plane anisotropy. This could be understood with the effective magnetic field interacting with electron spins, which can be expressed as $B_{\text{eff}} = \frac{1}{2m_e c^2} \mathbf{p} \times \nabla V$, where \mathbf{p} is the momentum and ∇V is the potential gradient. m_e is the electron mass and c is the speed of light. For 2D materials, \mathbf{p} is always in the in-plane (x - y) direction. On the other hand, since monolayer TMDs has a horizontal mirror plane \mathcal{M}^z , the out-of-plane component of potential gradient ∇V is tiny. As a result, B_{eff} is mainly along the out-of-plane direction, leading to the Zeeman type spin splitting. These arguments are verified by the BZ

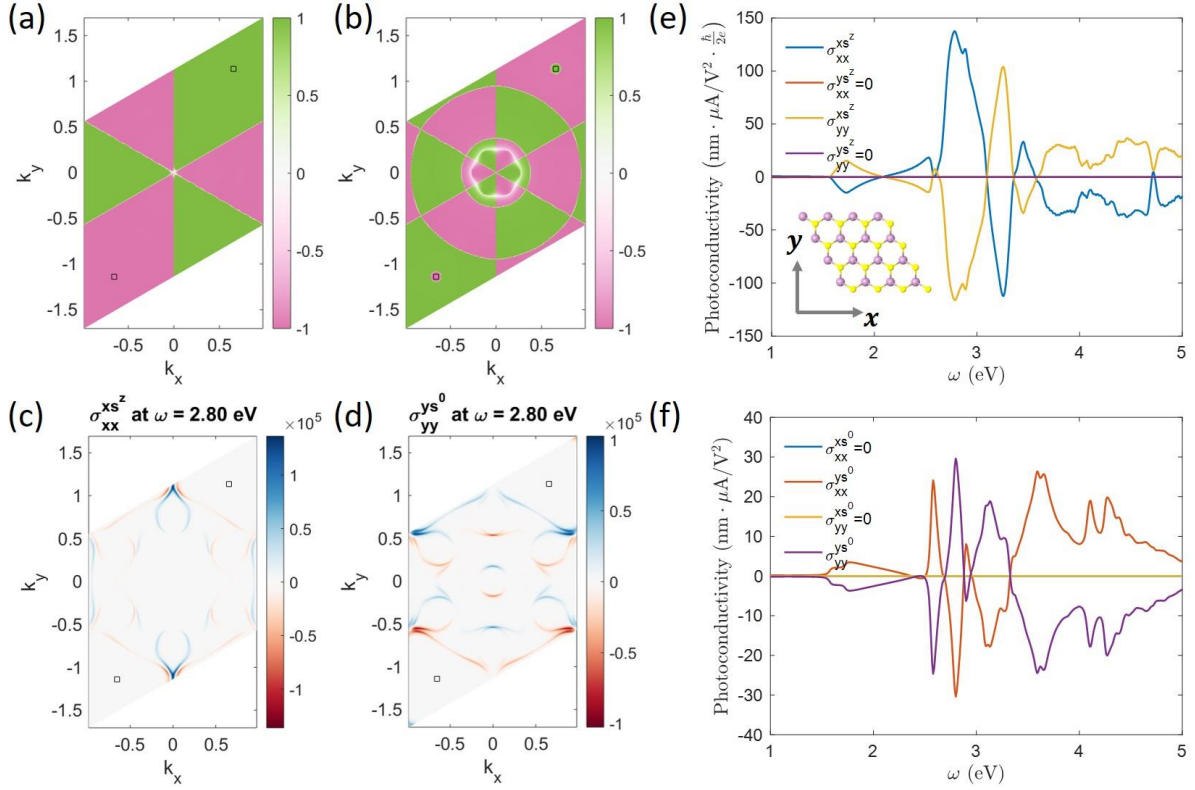


Figure 2 NLO spin current of MoS2 (a-b) The spin- z component $s_{mm}^z(\mathbf{k})$ over the BZ for the (a) highest valence band and (b) lowest conduction band of MoS2. Nearly all k -points have $s_{mm}^z(\mathbf{k}) \cong \pm 1$. The spin-valley locking can also be seen. **(c-d)** k -specified contribution to the total photoconductivity $\sigma_{xx}^{xs^z}$ and $\sigma_{yy}^{ys^0}$. The black boxes in (a-d) indicate K and K' points. **(e-f)** The NLO spin- z and charge conductivity. The complementary behavior is clearly observable: the spin and charge currents are in perpendicular directions. Inset of (e): the atomic structure of MoS2.

distribution of the spin- z component $s_{mm}^z(\mathbf{k}) = \langle m\mathbf{k} | \sigma_z | m\mathbf{k} \rangle$ from *ab initio* calculations with SOC. Figures 2(a) and 2(b) show $s_{mm}^z(\mathbf{k})$ for the highest valence band and the lowest conduction band of MoS₂, respectively. One can see that $s_{mm}^z(\mathbf{k}) \cong \pm 1$ for nearly all k -points. Also, $s_{mm}^z(\mathbf{k})$ is valley-dependent and is opposite near the K and K' valleys, which is the spin-valley locking^{36,37}.

We take monolayer 2H MoS₂ as an example to calculate the NLO spin current. The atomic structure of MoS₂ (space group $P\bar{6}m2$) is shown in the inset of Figure 2(e), which is invariant under \mathcal{M}^x and \mathcal{M}^z . Here we need to examine constraints on NLO spin or charge current from mirror symmetry \mathcal{M}^d . The polar vector v^a satisfies $\mathcal{M}^d v^a(\mathbf{k}) = (-1)^{\delta_{da}} v^a(\mathbf{k}')$, where \mathbf{k}' is the image of \mathbf{k} under \mathcal{M}^d (only the d -th component flip its sign), whereas the axial vector s^i should satisfy $\mathcal{M}^d s^i(\mathbf{k}) = -(-1)^{\delta_{di}} s^i(\mathbf{k}')$. Therefore, one has $\mathcal{M}^d N^{0abc}(\mathbf{k}) = -N^{0abc}(\mathbf{k}')$ when there are *odd* number of d within a, b and c , and the charge current should vanish in this case. For

example, when the system has \mathcal{M}^x , then σ_{xx}^{x,s^0} and σ_{yy}^{x,s^0} should vanish. On the other hand, if $d \neq i$, the spin- i current should vanish when there are *even* number of d within a, b and c , because the \mathcal{M}^d operation on s^i contributes to an additional sign change. Therefore, σ_{xx}^{x,s^z} and σ_{yy}^{x,s^z} could exist in the presence of \mathcal{M}^x . Due to the opposite behavior of N^{0abc} and N^{iabc} under \mathcal{M}^d , a pure spin current can be generated if the system possesses \mathcal{M}^d .

The NLO spin and charge conductivity of monolayer 2H MoS₂ under different light polarizations are shown in Figure 2(e-f). One can see that with in-plane polarized light, the nonzero conductivities are complementary for spin and charge currents. In detail, under the x -polarized light, the charge current is along y -direction ($\sigma_{xx}^{x,s^0} = 0$ and $\sigma_{xx}^{y,s^0} \neq 0$), whereas the spin- z currents is along the x -direction ($\sigma_{xx}^{x,s^z} \neq 0$ and $\sigma_{xx}^{y,s^z} = 0$). This indicates that there are indeed carriers moving along the x -direction, but spin up and spin down electrons are moving oppositely (along x and $-x$), so they compensate with each other and the net charge flux is zero. However, there is a net spin current. Along y direction, the spin up and spin down carriers move together, leading to zero spin current (Figure 1). Similar effects occur as well in the case of y -polarized light. These results are consistent with the symmetry analysis above. Interestingly, the spin- z conductivity can be larger than the charge conductivity (in the sense of equivalating $\frac{\hbar}{2} = e$), indicating that the hidden carrier movements are actually rapid. We also plot the k -specified contribution to the total conductivity, defined as $I_{bc}^{a,s^i}(\omega, \mathbf{k}) = \sum_{mnl} \frac{f_{lm} v_{lm}^b}{E_{ml} - \hbar\omega + i\delta} \left(\frac{j_{mn}^{a,s^i} v_{nl}^c}{E_{mn} + i\delta} - \frac{v_{mn}^c j_{nl}^{a,s^i}}{E_{nl} + i\delta} \right)$, in Figure 2(c-d) for σ_{xx}^{x,s^z} and σ_{yy}^{y,s^0} at $\omega = 2.8$ eV. The mirror symmetry $k_x \rightarrow -k_x$ can be clearly observed.

Bilayer Anti-ferromagnetic MnBi₂Te₄. Next, we study the bilayer AFM MnBi₂Te₄ (MBT)^{38,39}, where large NLO charge current has been reported^{40,41}. Each single layer of MBT is composed of a septuple atomic layer (SL) in the sequence of Te-Bi-Te-Mn-Te-Bi-Te. In each SL, the Mn atom possesses magnetic moments $\sim 5 \mu_B$, and two SLs are in-plane ferromagnetically coupled. The bulk MBT is van der Waals (vdW) stacked SLs, which is an AFM topological

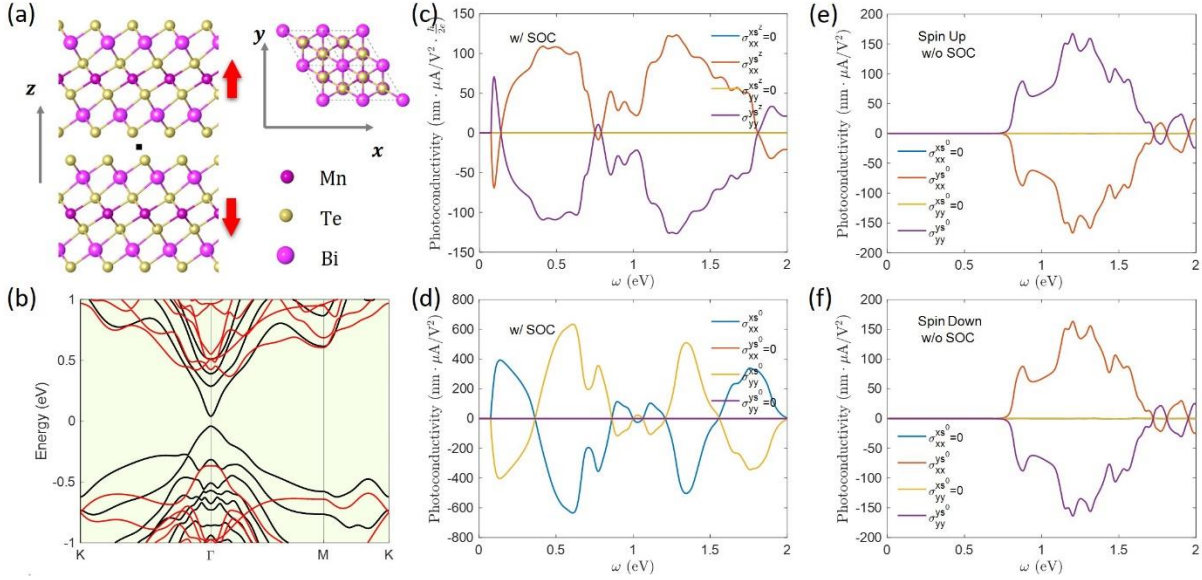


Figure 3. NLO spin current of MBT (a) Atomic structure of bilayer MnBi_2Te_4 . The atomic structure has both inversion symmetry \mathcal{P} and mirror symmetry \mathcal{M}^x . The inversion center is in between the two layers (black square). The magnetic momentum is indicated by the red arrows. Considering magnetism, both \mathcal{P} and \mathcal{M}^x break. (b) Band structure of MBT with (black) and without (red) SOC. (c-d) The NLO spin and charge photoconductivity of bilayer MnBi_2Te_4 with SOC. Both spin and charge currents have nonzero components and exhibit complementary behavior. (e-f) The NLO charge conductivity without SOC. The spin up and down states are treated separately. The photoconductivity from spin up and down states are exactly opposite to each other. Therefore, the total charge conductivity is zero. But the spin-z conductivity is nonzero.

insulator, and the AFM nature persists when MBT is thinned down to multiple atomic layers. In particular, bilayer MBT is a compensated AFM insulator, whose atomic structure is shown in Figure 3(a). The ground state magnetic moments are pointing along the z direction with a magnetic point group of $\bar{3}'m'$. The atomic site structure of bilayer MBT is invariant under \mathcal{P} and the inversion center lies in the vdW gap between the two layers (black square in Figure 3a). However, when one considers magnetism, both \mathcal{P} and \mathcal{T} are broken. Nevertheless, the AFM bilayer MBT system is invariant under \mathcal{PT} . Similarly, we find that \mathcal{PM}^x is also preserved. According to previous analysis, we know that $\mathcal{PM}^d v^a(\mathbf{k}) = -(-1)^{\delta_{ab}} v^a(-\mathbf{k}')$ and $\mathcal{PM}^d s^i(\mathbf{k}) = -(-1)^{\delta_{ai}} s^i(-\mathbf{k}')$. Then, one can see that when $d \neq i$, N^{0abc} (N^{iabc}) should vanish after BZ integration when there are even (odd) number of d within a, b and c . Therefore, one can still obtain a pure spin current in systems with \mathcal{PM}^d , and the nonvanishing components of charge and spin currents are interchanged between systems with \mathcal{M}^d and \mathcal{PM}^d .

The band structures of bilayer MBT with and without SOC are shown in Figure 3(b). When SOC effect is included, the bandgap is about 0.1 eV and is located at the Γ point, whereas it is

about 0.7 eV and is indirect without SOC. As shown in Figure 3(c-f), the SOC also makes a significant difference on the NLO spin and charge conductivity. When SOC is turned off, s^z is a good quantum number. States with $s^z = \pm 1$ are strictly degenerate in an AFM system and can be treated separately. The results are shown in Figure 3(e-f), where one can see that the charge current from spin up (j_\uparrow) and down (j_\downarrow) states are exactly opposite to each other. Consequently, the total charge current $j^{s^0} = j_\uparrow + j_\downarrow$ is zero. However, the total spin-z current is $j^{s^z} = j_\uparrow - j_\downarrow$ and is nonzero. Therefore, a pure spin current without any charge current is predicted. These results are consistent with the those in Ref. ²¹, where several other well-known AFM materials such as NiO and BiFeO₃ were studied.

However, SOC would break the spin rotation symmetry^{41,42}. We find that when SOC is included, both spin-z and charge current can be nonzero and exhibit complementary behavior similar to that in the case of MoS₂. But since MBT has \mathcal{PM}^x while MoS₂ has \mathcal{M}^x , the nonzero components of charge and spin currents are interchanged between MBT and MoS₂, which can be observed when comparing Figure 2(e-f) with Figure 3(c-d). Therefore, one should expect a nonzero charge current perpendicular to the spin-z current in the MBT system as shown in Figure 3(c-d), which cannot be predicted without SOC effects.

Surface States of Topological Materials. Topological materials such as topological insulators⁴³⁻⁴⁵ (TIs) and topological semimetals^{46,47} have attracted intense interests in the recent years. In TIs, the bulk states are insulating with a finite bandgap, while the surface states are metallic with symmetry protected vanishing bandgap, which has potential applications in electronic and spintronic devices. One salient feature of the surface states is the spin-momentum locking, which could prevent the electrons from backscattering and facilitate spin manipulations⁴⁸⁻⁵⁰. In addition, the inversion symmetry \mathcal{P} is naturally broken on the surfaces, even if the bulk possesses \mathcal{P} . Therefore, the NLO charge⁵¹ and spin current can be induced solely on surfaces, while the bulk remains silent.

Here we take the topological crystalline insulator (TCI)^{52,53} SnTe as the exemplary material. The bulk SnTe has space group $Fm\bar{3}m$ so that is inversion symmetric, which forbids the NLO charge or spin currents. Here we consider the (001) surface, which has a four-fold rotational

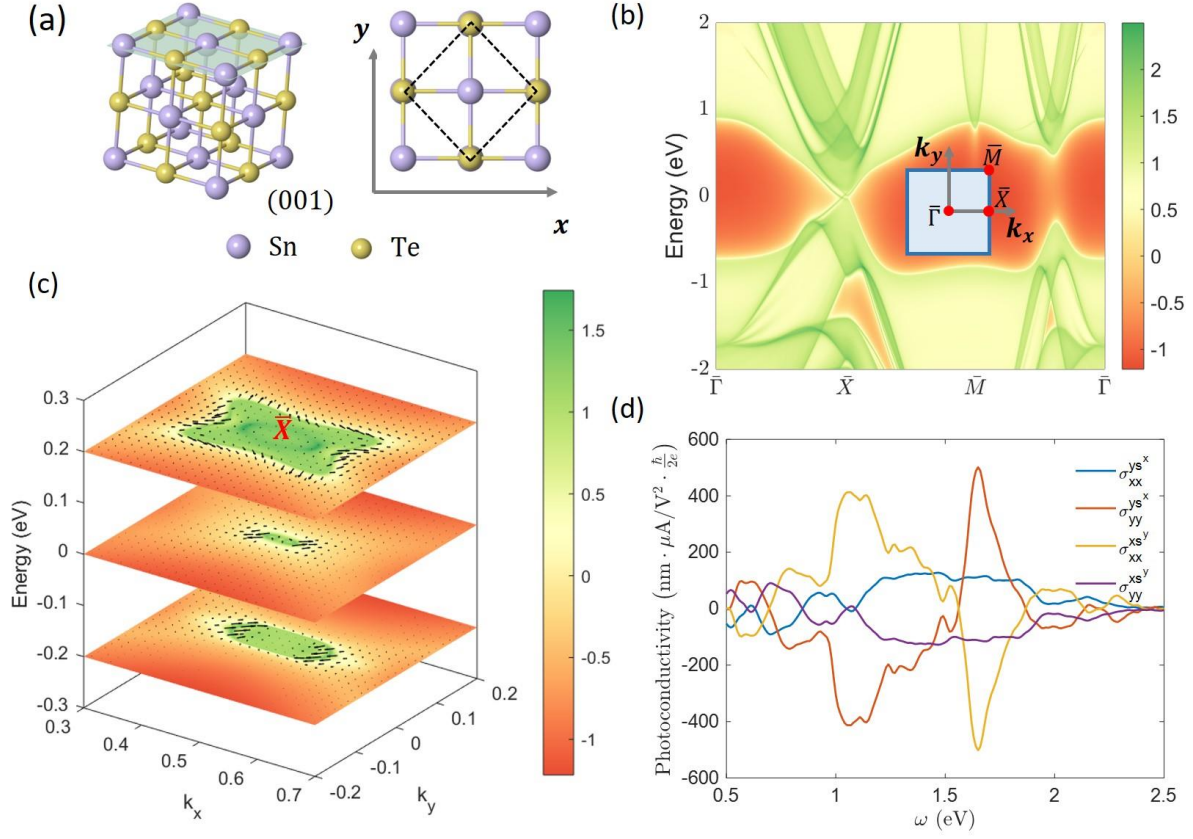


Figure 4. NLO spin current on the (001) surface of SnTe. (a) The atomic structure of SnTe. In the left panel the (001) face is painted in light green, which possesses two mirror symmetries \mathcal{M}^x and \mathcal{M}^y . The dashed box in the right panel indicates the primitive cell on the surface. (b) The surface spectrum function $A(\mathbf{k}, \omega)$ on high symmetry lines in the BZ. The gapless surface states can be observed. (c) The surface spectrum function $A(\mathbf{k}, \omega)$ over the BZ for selected $\omega = -0.2, 0$, and 0.2 eV. k_x and k_y are in the unit of reciprocal lattices. The surface spin textures are indicated by the black arrows. Color scheme (red to green) in (b) and (c) represents surface state contribution. The color bars are in logarithmic scale, and the energy is offset to the valence band maximum. (d) The NLO spin current conductivity with x and y spin polarizations. Note that all charge and spin- z current components are vanishing due to \mathcal{M}^x and \mathcal{M}^y .

symmetry and two mirror symmetries \mathcal{M}^x and \mathcal{M}^y (Figure 4a). The spectrum function $A(\mathbf{k}, \omega)$ of the (001) surface is obtained with iterative Green's function method^{54,55} and are shown in Figure 4(b-c). In Figure 4(b), $A(\mathbf{k}, \omega)$ along high symmetry lines in the BZ with varying ω is presented, and the gapless surface states can be clearly observed. In Figure 4(c), $A(\mathbf{k}, \omega)$ near \bar{X} point in the BZ with selected energy $\omega = -0.2, 0$, and 0.2 eV are plotted. One can see that $A(\mathbf{k}, \omega)$ can have significant values on the same k -point with different ω , enabling strong interband transitions and significant photocurrents. In addition, the surface spin textures are plotted as black

arrows. The nonzero s^x and s^y components indicate that one can obtain spin- x and spin- y currents.

According to our previous symmetry analysis, under in-plane polarized light ($b, c = x$ or y), no NLO charge or spin- z current can be generated on the (001) surface. However, it is possible to have nonzero spin- x and spin- y currents, which is verified by our *ab initio* calculations. We use a slab model to compute the surface contributed NLO spin and charge conductivity. In order to distinguish the contribution from only one surface of the slab, we define a projection operator⁵⁶ $P_l = \sum_{i \in l} |\psi_i\rangle\langle\psi_i|$. Here $|\psi_i\rangle$ are maximally localized Wannier functions (MLWFs), and the summation runs over MLWFs whose Wannier centers locate on the l -th atomic layer. Then we replace the current operator j in Eq. (2) with $P_l j P_l$, and the resultant conductivity can be layer distinguished (on the l -th layer). Note that there could have nonzero cross-terms $P_l j P_m$ (with $l \neq m$) contribution, indicating the interference between the l -th and m -th layer. We test that even for neighboring layers with $m = l \pm 1$, the contribution from $P_l j P_m$ is quite small (less than 10 %). Here for a conceptual demonstration of our theory, we only consider $P_{l=1} j P_{l=1}$ and calculate the contribution from the out-most layer. NLO spin- x and spin- y conductivities are plotted in Figure 4(d). One can see that the maximum value of $\sigma_{yy}^{ys^x}$ can reach $500 \text{ nm} \cdot \mu\text{V}/\text{\AA}^2 \cdot \frac{\hbar}{2e}$. We would like to emphasize that the under light field with in-plane polarization, NLO charge current is absent on this (001) surface, therefore a pure spin current without any charge current at all can be generated. Such methodology can also be used to distinguish surface and bulk states and to probe the surface states.

Table 2 Mechanisms for charge and spin current generation under different symmetry conditions.

	\mathcal{P} -conserved	\mathcal{P} -broken \mathcal{T} -conserved	\mathcal{P} -broken, \mathcal{T} -broken \mathcal{PT} -conserved	\mathcal{P} -broken, \mathcal{T} -broken \mathcal{PT} -broken
Charge Current	No	LPL \Leftrightarrow Shift CPL \Leftrightarrow Injection	LPL \Leftrightarrow Injection CPL \Leftrightarrow Shift	LPL \Leftrightarrow Shift+Injection CPL \Leftrightarrow Shift+Injection
Spin Current	No	LPL \Leftrightarrow Injection CPL \Leftrightarrow Shift	LPL \Leftrightarrow Shift CPL \Leftrightarrow Injection	LPL \Leftrightarrow Shift+Injection CPL \Leftrightarrow Shift+Injection

Discussions. Before concluding, we would like to make some remarks. As we discussed before, the real and imaginary parts of Eq. (2) are conductivities under LPL and CPL, respectively. For a charge current in a \mathcal{P} -broken but \mathcal{T} -conserved system, they are the well-known shift and injection mechanisms. In this case, only the *imaginary* part of the numerator N^{0abc} contributes to the total conductivity, while the denominator $D = \frac{1}{(\omega_{ml}-\omega+i/\tau)(\omega_{mn}+i/\tau)}$ can be separated into real $\text{Re}(D)$ and imaginary $\text{Im}(D)$ parts. The usual formulae for shift and injection current conductivity correspond to $N^{0abc}\text{Im}(D)$ and $N^{0abc}\text{Re}(D)$, respectively. On the other hand, for a spin current, it is the *real* part of the numerator N^{iabc} that contributes to the total conductivity. Therefore, the spin conductivity under LPL and CPL should correspond to $N^{iabc}\text{Re}(D)$ and $N^{iabc}\text{Im}(D)$, which are injection and shift mechanisms, respectively. Therefore, the mechanisms for generating currents under LPL and CPL are interchanged between spin and charge currents. Particularly, in \mathcal{T} -conserved system, the shift mechanism for spin current should vanish under LPL, consistent with the arguments in Ref. ²². Similar analysis can be applied to systems with \mathcal{P} - and \mathcal{T} -broken but \mathcal{PT} -conserved^{40,42}, and the results are listed in Table 2. Finally, for a system with neither \mathcal{P} , \mathcal{T} nor \mathcal{PT} , there are no symmetry constraints anymore and both shift and injection mechanisms can induce spin and charge currents under LPL and CPL.

Conclusion. In conclusion, we demonstrate a general picture of spin photocurrent generation with nonlinear light-matter interactions. Such bulk spin photovoltaic effect (BSPE) only requires inversion symmetry breaking in the crystal and is applicable to a wide range of materials and extended defects like surfaces, stacking faults, grain boundaries and dislocations. By symmetry analysis, we reveal that if the system possesses mirror symmetry or inversion-mirror symmetry, a pure spin current can be realized. Our theory is verified with *ab initio* calculations on several distinct material systems, and the spin current conductivity is found to be gigantic, comparable or even bigger than its bulk photovoltaic effect (BPVE) and circular photogalvanic effect (CPGE) cousins. The predicted BSPE and light induced pure spin current may find applications in next generation energy efficient and ultrafast spintronics and quantum information processing.

Methods The first-principles calculations are based on density functional theory (DFT)^{57,58} as implemented in Vienna *ab initio* simulation package (VASP)^{59,60}. The exchange-correlation interactions is treated by a generalized gradient approximation (GGA) in the form of Perdew-Burke-Ernzerhof (PBE)⁶¹. Core and valence electrons are treated by projector augmented wave

(PAW) method⁶² and plane-wave basis functions, respectively. For DFT calculations, the first Brillouin zone is sampled by a Γ -centered \mathbf{k} -mesh with grid density of at least $2\pi \times 0.02 \text{ \AA}^{-1}$ along each dimension. The DFT+U method is adopted to treat the d orbitals of Mn atoms in MBT ($U = 4.0 \text{ eV}$). The maximally-localized Wannier functions (MLWF) are generated with the Bloch waves from DFT calculations as implemented in the Wannier90 package⁶³. Then a tight-binding (TB) Hamiltonian is constructed from the MLWF, which is utilized to calculate the NLO charge and spin conductivity according to Eq. (2). The k -mesh convergence for BZ integration is well tested.

Acknowledgments. This work was supported by an Office of Naval Research MURI through grant #N00014-17-1-2661.

References

1. Žutić, I., Fabian, J. & Sarma, S. Das. Spintronics: Fundamentals and applications. *Reviews of Modern Physics* **76**, 323–410 (2004).
2. Bader, S. D. & Parkin, S. S. P. Spintronics. *Annu. Rev. Condens. Matter Phys.* **1**, 71–88 (2010).
3. Shor, P. W. Algorithms for quantum computation: discrete logarithms and factoring. in 124–134 (Institute of Electrical and Electronics Engineers (IEEE), 2002). doi:10.1109/sfcs.1994.365700
4. Ladd, T. D. *et al.* Quantum computers. *Nature* **464**, 45–53 (2010).
5. Umesh, S. & Mittal, S. A survey of spintronic architectures for processing-in-memory and neural networks. *Journal of Systems Architecture* **97**, 349–372 (2019).
6. Awschalom, D. D. & Flatté, M. E. Challenges for semiconductor spintronics. *Nature Physics* **3**, 153–159 (2007).
7. Ganichev, S. D. *et al.* Spin-galvanic effect. *Nature* **417**, 153–156 (2002).
8. Benítez, L. A. *et al.* Tunable room-temperature spin galvanic and spin Hall effects in van der Waals heterostructures. *Nat. Mater.* **19**, 170–175 (2020).
9. Sinova, J., Valenzuela, S. O., Wunderlich, J., Back, C. H. & Jungwirth, T. Spin Hall effects. *Rev. Mod. Phys.* **87**, 1213–1260 (2015).
10. D’Yakonov, M. I., Perel’, V. I., D’Yakonov, M. I. & Perel’, V. I. Possibility of Orienting Electron Spins with Current. *JETPL* **13**, 467 (1971).
11. Dyakonov, M. I. & Perel, V. I. Current-induced spin orientation of electrons in semiconductors. *Phys. Lett. A* **35**, 459–460 (1971).
12. Ando, K. *et al.* Inverse spin-Hall effect induced by spin pumping in metallic system. in *Journal of Applied*

- Physics* **109**, 103913 (American Institute of PhysicsAIP, 2011).
13. Uchida, K. *et al.* Observation of the spin Seebeck effect. *Nature* **455**, 778–781 (2008).
 14. Adachi, H., Uchida, K., Saitoh, E. & Maekawa, S. Theory of the spin Seebeck effect. *Reports Prog. Phys.* **76**, 036501 (2013).
 15. Sheng, P. *et al.* The spin Nernst effect in tungsten. *Sci. Adv.* **3**, e1701503 (2017).
 16. Meyer, S. *et al.* Observation of the spin Nernst effect. *Nat. Mater.* **16**, 97–981 (2017).
 17. Ganichev, S. D. *et al.* Conversion of spin into directed electric current in quantum wells. *Phys. Rev. Lett.* **86**, 4358–4361 (2001).
 18. Stevens, M. J. *et al.* Quantum Interference Control of Ballistic Pure Spin Currents in Semiconductors. *Phys. Rev. Lett.* **90**, 4 (2003).
 19. Hübner, J. *et al.* Direct Observation of Optically Injected Spin-Polarized Currents in Semiconductors. *Phys. Rev. Lett.* **90**, 4 (2003).
 20. Luo, Y. K. *et al.* Opto-valleytronic spin injection in monolayer MoS₂/few-layer graphene hybrid spin valves. *Nano Lett.* **17**, 3877–3883 (2017).
 21. Young, S. M., Zheng, F. & Rappe, A. M. Prediction of a linear spin bulk photovoltaic effect in antiferromagnets. *Phys. Rev. Lett.* **110**, 057201 (2013).
 22. Kim, K. W., Morimoto, T. & Nagaosa, N. Shift charge and spin photocurrents in Dirac surface states of topological insulator. *Phys. Rev. B* **95**, 035134 (2017).
 23. McIver, J. W., Hsieh, D., Steinberg, H., Jarillo-Herrero, P. & Gedik, N. Control over topological insulator photocurrents with light polarization. *Nat. Nanotechnol.* **7**, 96–100 (2012).
 24. Yuan, H. *et al.* Generation and electric control of spin-valley-coupled circular photogalvanic current in WSe₂. *Nat. Nanotechnol.* **9**, 851–857 (2014).
 25. Dhara, S., Mele, E. J. & Agarwal, R. Voltage-tunable circular photogalvanic effect in silicon nanowires. *Science (80-.)*. **349**, 726–729 (2015).
 26. Ji, Z. *et al.* Spatially dispersive circular photogalvanic effect in a Weyl semimetal. *Nat. Mater.* **18**, 955–962 (2019).
 27. De Juan, F., Grushin, A. G., Morimoto, T. & Moore, J. E. Quantized circular photogalvanic effect in Weyl semimetals. *Nat. Commun.* **8**, 1–7 (2017).
 28. Zhang, X., Liu, Q., Luo, J. W., Freeman, A. J. & Zunger, A. Hidden spin polarization in inversion-symmetric bulk crystals. *Nat. Phys.* **10**, 387–393 (2014).
 29. Lin, Z., Wang, C., Xu, Y. & Duan, W. Hidden Physical Effects in Non-centrosymmetric Crystals. (2020).
 30. Bernevig, B. A. & Zhang, S. C. Quantum spin hall effect. *Phys. Rev. Lett.* **96**, 106802 (2006).
 31. Kraut, W. & Von Baltz, R. Anomalous bulk photovoltaic effect in ferroelectrics: A quadratic response theory. *Phys. Rev. B* **19**, 1548–1554 (1979).
 32. Von Baltz, R. & Kraut, W. Theory of the bulk photovoltaic effect in pure crystals. *Phys. Rev. B* **23**, 5590–5596 (1981).
 33. Sinova, J. *et al.* Universal intrinsic spin Hall effect. *Phys. Rev. Lett.* **92**, 126603 (2004).

34. Fei, R., Lu, X. & Yang, L. Intrinsic Spin Photogalvanic Effect in Nonmagnetic Insulator. (2020).
35. Laturia, A., Van de Put, M. L. & Vandenberghe, W. G. Dielectric properties of hexagonal boron nitride and transition metal dichalcogenides: from monolayer to bulk. *npj 2D Mater. Appl.* **2**, 1–7 (2018).
36. Zeng, H. *et al.* Optical signature of symmetry variations and spin-valley coupling in atomically thin tungsten dichalcogenides. *Sci. Rep.* **3**, 1–5 (2013).
37. Bawden, L. *et al.* Spin-valley locking in the normal state of a transition-metal dichalcogenide superconductor. *Nat. Commun.* **7**, 1–6 (2016).
38. Li, J. *et al.* Intrinsic magnetic topological insulators in van der Waals layered MnBi₂Te₄-family materials. *Sci. Adv.* **5**, eaaw5685 (2019).
39. Deng, Y. *et al.* Quantum anomalous Hall effect in intrinsic magnetic topological insulator MnBi₂Te₄. *Science (80-.)*. **367**, 895–900 (2020).
40. Wang, H. & Qian, X. Giant nonlinear photocurrent in \mathcal{PT} -symmetric magnetic topological quantum materials. (2020).
41. Fei, R., Song, W. & Yang, L. Giant linearly-polarized photogalvanic effect and second harmonic generation in two-dimensional axion insulators. (2020).
42. Zhang, Y. *et al.* Switchable magnetic bulk photovoltaic effect in the two-dimensional magnet CrI₃. *Nat. Commun.* **10**, 1–7 (2019).
43. Hasan, M. Z. & Kane, C. L. Colloquium: Topological insulators. *Rev. Mod. Phys.* **82**, 3045–3067 (2010).
44. Qi, X. L. & Zhang, S. C. Topological insulators and superconductors. *Rev. Mod. Phys.* **83**, (2011).
45. Bansil, A., Lin, H. & Das, T. Colloquium: Topological band theory. *Rev. Mod. Phys.* **88**, (2016).
46. Armitage, N. P., Mele, E. J. & Vishwanath, A. Weyl and Dirac semimetals in three-dimensional solids. *Rev. Mod. Phys.* **90**, (2018).
47. Yan, B. & Felser, C. Topological Materials: Weyl Semimetals. *Annu. Rev. Condens. Matter Phys.* **8**, 337–354 (2017).
48. Tian, J., Hong, S., Miotkowski, I., Datta, S. & Chen, Y. P. Observation of current-induced, long-lived persistent spin polarization in a topological insulator: A rechargeable spin battery. *Sci. Adv.* **3**, e1602531 (2017).
49. Mellnik, A. R. *et al.* Spin-transfer torque generated by a topological insulator. *Nature* **511**, 449–451 (2014).
50. Lin, B. C. *et al.* Electric Control of Fermi Arc Spin Transport in Individual Topological Semimetal Nanowires. *Phys. Rev. Lett.* **124**, 116802 (2020).
51. Chang, G. *et al.* Unconventional Photocurrents from Surface Fermi Arcs in Topological Chiral Semimetals. *Phys. Rev. Lett.* **124**, 166404 (2020).
52. Fu, L. Topological crystalline insulators. *Phys. Rev. Lett.* **106**, 106802 (2011).
53. Hsieh, T. H. *et al.* Topological crystalline insulators in the SnTe material class. *Nat. Commun.* **3**, 1–7 (2012).
54. Sancho, M. P. L., Sancho, J. M. L. & Rubio, J. Quick iterative scheme for the calculation of transfer matrices: application to Mo (100). *J. Phys. F Met. Phys.* **14**, 1205 (1984).

55. Sancho, M. P. L., Sancho, J. M. L., Sancho, J. M. L. & Rubio, J. Highly convergent schemes for the calculation of bulk and surface Green functions. *J. Phys. F Met. Phys.* **15**, 851 (1985).
56. Varnava, N. & Vanderbilt, D. Surfaces of axion insulators. *Phys. Rev. B* **98**, 245117 (2018).
57. Hohenberg, P. & Kohn, W. Inhomogeneous Electron Gas. *Phys. Rev.* **136**, B864–B871 (1964).
58. Kohn, W. & Sham, L. J. Self-Consistent Equations Including Exchange and Correlation Effects. *Phys. Rev.* **140**, A1133–A1138 (1965).
59. Kresse, G. & Furthmüller, J. Efficiency of ab-initio total energy calculations for metals and semiconductors using a plane-wave basis set. *Comput. Mater. Sci.* **6**, 15–50 (1996).
60. Kresse, G. & Furthmüller, J. Efficient iterative schemes for *ab initio* total-energy calculations using a plane-wave basis set. *Phys. Rev. B* **54**, 11169–11186 (1996).
61. Perdew, J. P., Burke, K. & Ernzerhof, M. Generalized Gradient Approximation Made Simple. *Phys. Rev. Lett.* **77**, 3865–3868 (1996).
62. Blöchl, P. E. Projector augmented-wave method. *Phys. Rev. B* **50**, 17953–17979 (1994).
63. Mostofi, A. A. *et al.* An updated version of wannier90: A tool for obtaining maximally-localised Wannier functions. *Comput. Phys. Commun.* **185**, 2309–2310 (2014).